

Terahertz Magnetic and Lattice Excitations in van der Waals Ferromagnet VI_3

Dávid Hovančík^{1*}, Dalibor Repček^{2,3}, Fedir Borodavka², Christelle Kadlec², Karel Carva¹, Petr Doležal¹, Marie Kratochvílová¹, Petr Kužel², Stanislav Kamba², Vladimír Sechovský¹, Jiří Pospíšil¹

¹Charles University, Faculty of Mathematics and Physics, Department of Condensed Matter Physics, Ke Karlovu 5, 121 16 Prague 2, Czech Republic

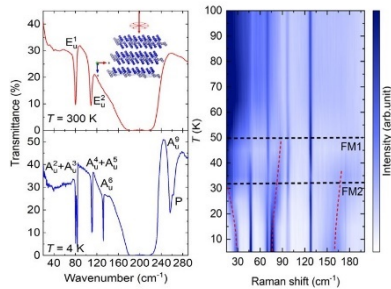
²Institute of Physics, Czech Academy of Sciences, Na Slovance 2, 182 21 Prague 8, Czech Republic

³Faculty of Nuclear Sciences and Physical Engineering, Czech Technical University in Prague, Břehová 7, 115 19 Prague 1, Czech Republic

Corresponding Author Email: hovancik@mag.mff.cuni.cz

Abstract: We use the synergy of infrared, terahertz, and Raman spectroscopies with DFT calculations to shed light on the magnetic and lattice properties of VI_3 . The structural transition at $T_{S1} = 79$ K is accompanied by a large splitting of polar phonon modes. Below T_{S1} , strong ferromagnetic fluctuations are observed. The variations of phonon frequencies at 55 K induced by magnetoelastic coupling enhanced by spin-orbit interaction indicate the proximity of long-range ferromagnetic order. Below $T_C = 50$ K, two Raman modes simultaneously appear and show dramatic softening in the narrow interval around the temperature T_{S2} of the second structural transition associated with the order-order magnetic phase transition. Below T_{S2} , a magnon in the THz range appears in Raman spectra. The THz magnon observed in VI_3 indicates the application potential of 2D van der Waals ferromagnets in ultrafast THz spintronics, which has previously been considered an exclusive domain of antiferromagnets.

TOC Graphic



Magnetic van der Waals (vdW) materials have become a target of intense basic and applied research due to the high potential for microelectronics and spintronics. These include the transition metal (T) trihalides TX_3 (X – halogen)¹ which share an X - T - X triple-layer structure motif consisting of a graphene-like honeycomb network of T atoms in the ab plane interposed between two layers

of X atoms. The triple-layers are stacked on top of each other and the neighboring halogen atom layers in the sequence $\dots X$ - T - X - X - T - X \dots are separated by a vdW gap.

CrI_3 , the most intensively studied TX_3 compound, is an Ising-type ferromagnetic (FM) semiconductor with $T_C = 61$ K². VI_3 adopts a trigonal structure ($R\bar{3}$ space group)

at room temperature (see Figure S1, S2 and S3) and then, upon cooling, it undergoes a first-order transition to the monoclinic phase at $T_{S1} = 79$ K³⁻⁵ and becomes FM at $T_C = 50$ K (see Figure S4) while keeping the monoclinic symmetry. The transition from the monoclinic to a triclinic structure ($P\bar{1}$ space group) at $T_{S2} = 32$ K is associated with the transformation from one FM structure to another⁶⁻⁹. These structural phase transitions are associated with distortions of the V honeycomb networks and minute changes in the V-V distances^{8,9}.

The measured ordered V magnetic moment in VI_3 ($\sim 1.24 \mu_B$ at 4 K)⁹ (see Figure S4) is significantly smaller than the expected spin-only moment of a V^{3+} ion ($2 \mu_B$) and tilted from the V honeycomb network's normal by $\sim 40^\circ$ ^{10,11}. When decreasing temperature from 50 K to 30 K the in-plane moment component gradually rotates within the ab -plane¹¹ - in total by 90° ⁹. The complex magneto-crystalline anisotropy together with the reduced V^{3+} magnetic moment can be attributed to the breaking of the three-fold symmetry in the monoclinic and triclinic phases, to a large orbital moment of V^{3+} ion, and spin-orbit coupling in both V^{3+} and Γ ions¹².

Similar to the CrI_3 case², a closer inspection of crystallographic and magnetic data collected on VI_3 provides indications of strong magneto-elastic coupling (MEC) as a key underlying mechanism of the observed unusual phenomena. In particular, the crystallographic phase transition at T_{S1} induces a change of magnetization in the paramagnetic state far above T_C ^{3,4,6}, and also the transition temperature T_{S1} can be controlled by the applied magnetic field⁷. The structural phase transition observed at 32 K and the aforementioned magnetic phase transition are interconnected via a strong MEC.

Raman scattering has proven to be an effective tool for investigating the magnetic and lattice degrees of freedom in 2D magnets¹³. Although it directly probes the optical phonons, the phenomena such as MEC, zone-folding, or magneto-optical Raman effect^{14,15} provide additional information about magnetism¹⁶⁻¹⁸. The Raman study by Lyu et al.¹⁹ performed on exfoliated flakes of VI_3 revealed the presence of a spin-wave excitation (magnon) and a two-magnon mode in the FM phase. Likewise, the signatures of FM order were spotted using polarization-resolved Raman scattering. Furthermore, the large quasi-elastic (QES) scattering around the temperature of the structural transition $T_{S1} = 79$ K has been identified. None of those features has yet been detected in the bulk crystal. Infrared (IR) spectroscopy data complementary to Raman scattering data are also lacking²⁰. In the case of VI_3 , such a lack of information caused a misinterpretation of the crystallographic phases and phase transitions¹⁹.

In this work, we used the complementarity of IR, terahertz (THz), and Raman spectroscopies to study the signatures of structural and magnetic phases in the bulk VI_3 single crystal at temperatures down to 4 K. This approach has allowed us to obtain a complete picture of the phonon modes in VI_3 , which can be compared to first principles predictions. We found that at $T_{S1} = 79$ K doubly degenerate IR active modes split and two new modes appear due to the structure symmetry lowering. At T_C , clear signs of MEC in both Raman and IR spectra

together with the modification of Raman polarization selection rules for A_g modes reflect the formation of the FM phase. In Raman spectra, we have identified a high-frequency acoustic magnon emerging below T_{S2} . The frequencies of the observed magnon are three orders higher than those in conventional ferromagnets. In addition, two other Raman active modes associated with ferromagnetism in VI_3 simultaneously emerge below T_C . They dramatically change their frequency in the neighborhood of T_{S2} indicating unusual interplay of low-temperature magnetic and structural phase transitions.

The room-temperature IR transmittance spectrum of VI_3 shown in Figure 1a reveals two phonon modes located at 80 and 109 cm^{-1} . No transmittance is observed in the frequency range of 180-220 cm^{-1} , which is typical for the reststralen band²¹ with almost 100 % reflectivity. The edges of this band should correspond to the frequencies of the transverse and longitudinal phonon²². Using the results of our first-principles calculations for the $R\bar{3}$ rhombohedral phase^{4,7,23}, we assigned the symmetries of the phonons seen in Figure 1a.. The modes visible at 300 K were identified as doubly degenerate E_u modes oscillating in-plane. E_u^1 and E_u^2 show clear splitting upon cooling between 80 and 77.5 K (passing T_{S1}). Furthermore, the other three modes appear at 131, 256, and 262 cm^{-1} just below T_{S1} as seen in Figure 1c. The lifting of the phonon mode degeneracy reflects the crystal symmetry reduction due to the rhombohedral to monoclinic phase transition^{3,4,7,8,23,24}. The THz spectra measured at several temperatures (see Figure S5) confirmed the splitting of the E_u^1 mode at T_{S1} .

Given the point groups corresponding to the $R\bar{3}$ (C_{3i} point group), $C2/m$ (C_{2h} point group) and $P\bar{1}$ (C_i point group) space groups and the Wyckoff positions of V and I atoms^{5,7} we can consider the factor group analysis for zone-center optical phonons (see Table 1). The C_{3i} point group has 6 IR active modes ($3A_u + 3E_u$) and 8 Raman active modes ($4A_g + 4E_g$), the C_{2h} point group 9 IR active modes ($5A_u + 4B_u$) and 12 Raman active modes ($6A_g + 6B_g$), and the C_i point group 9 IR active A_u modes and 12 Raman active A_g modes.

Table 1: The irreducible representations of the optical phonons. The irreducible representations are given for D_{3d} , C_{3i} , C_{2h} , and C_i point group²⁵

| Point group | Irreducible representations for the optical modes |
|-------------------------|---|
| D_{3d} | $\Gamma_{optical} = 2A_{1g} + 2A_{2g} + 4E_g + A_{1u} + 2A_{2u} + 3E_u$ |
| C_{3i} ($R\bar{3}$) | $\Gamma_{optical} = 4A_g + 4E_g + 3A_u + 3E_u$ |
| C_{2h} ($C2/m$) | $\Gamma_{optical} = 6A_g + 6B_g + 4A_u + 5B_u$ |
| C_i ($P\bar{1}$) | $\Gamma_{optical} = 12A_g + 9A_u$ |

All doubly degenerate E_u and E_g phonon modes should split up at T_{S1} . The splitting of E_{2u} mode is quite weak just below T_{S1} such that only a shoulder (asymmetry) of the peak is observed; the splitting can be experimentally

resolved below ~ 55 K deeply in the monoclinic phase (see Figure 1c). This result can be understood by the subtle structural change at T_{S1} leaving certain two-dimensional modes almost “intact”. In other words, the splitting of the E_u^2 mode above 55 K is below the resolution of the spectrometer making it appear as a single peak.

Since the triple-layer of VI_3 has the D_{3d} point symmetry for both bulk phases with C_{3i} and C_{2h} point symmetry (no relation group-subgroup)²⁶, we can find the relations between the irreps of the normal modes (see Table S1). For simplicity, we will label the phonon

modes below T_{S1} using the irreps of the C_i point group. The splitting can be quantified by DFT calculations for the low-temperature structure (see Table 2.). The monoclinic symmetry below T_{S1} ^{3,7} permits distortions of the original V honeycomb layers that break the 3-fold rotation symmetry, namely dimerization or anti-dimerization²⁷. Son et al.³ have found evidence of anti-dimerization, while another work argues for dimerization⁸. Our previous computational study has shown that a significant perturbation of the 3-fold rotation symmetry as introduced by anti-dimerization is needed to explain the unusual angular dependence of

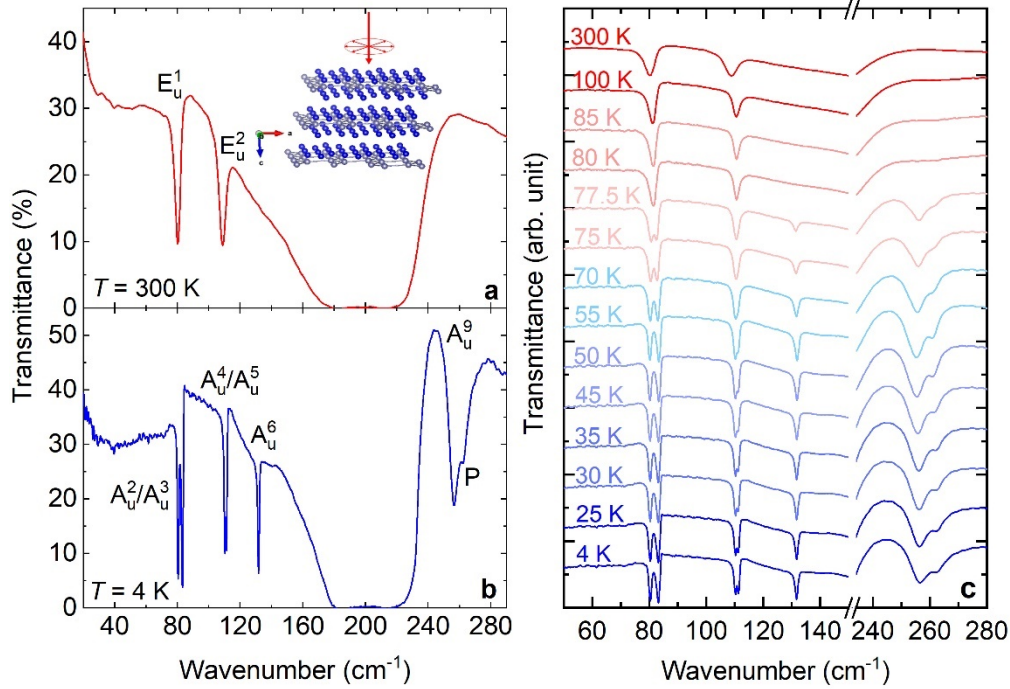


Figure 1: IR transmittance spectra of VI_3 single crystal. a) Assignment of the modes at 300 K and b) 4 K. c) Whole temperature dependence. The inset in 1. a) shows the orientation of the layers with respect to the incoming unpolarized beam. The crystal had the thickness of ~ 30 μm .

magnetic anisotropy energy in this system¹². We found out that the two new modes A_u^6 and A_u^9 observed below T_{S1} at 131 and 256 cm^{-1} (see Figure 1b.) correspond to the A_u^2 and A_u^3 modes (rhombohedral notation) that are not seen in the rhombohedral phase due to the sample orientation (see inset in Figure 1a.). The rapid increase in the activity of A_u^6 and A_u^9 mode can be explained by the first order phase transition at T_{S1} ²⁸. An additional peak P at 261 cm^{-1} , which also shows up below T_{S1} , does not correspond to any phonon mode in our calculated spectra (see Table 2.). It might possibly come from the splitting of the E_u^2 mode. However, such a large splitting is inconsistent with the subtle structural change at T_{S1} .

By fitting the spectral line shape of the phonon modes with a Lorentzian function we obtained the temperature-dependence of the mode frequencies shown in Figure 2. We noticed the mirrored splitting trend of E_u^1 and E_u^2

“daughter” modes $A_u^2+A_u^3$ and $A_u^4+A_u^5$ in the monoclinic phase. The observed splitting of the E_u^1 mode is rather consistent with the anti-dimerization picture which indicates that this distortion variant is present. The above-mentioned “daughter” modes and also the A_u^6 mode reverse the softening/hardening tendency at 55 K. This happens 5 K above T_C where short-range ferromagnetic order is expected in a 2D ferromagnet, which due to strong MEC may lead to slight shifts of phonon frequencies. In this context, it is worth noticing that VI_3 thin films²⁹, monolayer of VI_3 ³⁰ and also partly degraded surface layers of a bulk crystal^{31, 32} exhibit a higher value of T_C than bulk crystals. The temperature dependence of A_u^2 , A_u^3 , A_u^4 , and A_u^5 phonons reverse the trend again near 30 K, although less significantly. This could be considered as a signature of the second structural transformation from the monoclinic to triclinic phase⁷ conjugated with the change of FM order.

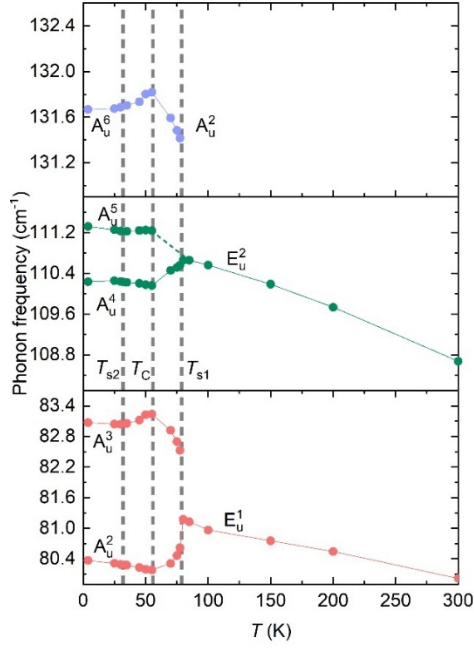


Figure 2: Temperature dependence of the phonon's frequencies. For the three selected IR active modes E_u^1 , E_u^2 and A_u^2 (silent in the rhombohedral phase). The solid vertical lines indicate the temperatures of high-temperature structural transition T_{s1} , ferromagnetic transition T_c and low-temperature structural transition T_{s2} .

Table 2: Calculated Γ -point optical phonon frequencies. For $R\bar{3}$ (C_{3i}) space group, monoclinic variant (C_{2h}) and triclinic dimerized (C_i) and anti-dimerized (C_i) version. The assignment to irreducible representations of C_{3i} and C_i point group is given.

| Phonon | Rhombohedral | | Monoclinic | | Triclinic | | Experiment (4 K) | |
|--------|-------------------------|-----------------------|--------------------|-----------------------------|------------------------|-------|---------------------|-------|
| | $R\bar{3}$ (C_{3i}) | Experiment (300 K) | (C_{2h}) | (C_i) Anti-dimerized | (C_i) dimerized | | | |
| | Irrep. | Freq (cm $^{-1}$) | Freq (cm $^{-1}$) | Irrep. | Freq (cm $^{-1}$) | | | |
| 1 | E_g^1 | 47.1 | 47.9 | 44.3 | A_g^1 | 38.0 | 41.0 | 47.9 |
| 2 | E_g^1 | 47.1 | 47.9 | 48.7 | A_g^2 | 49.4 | 49.5 | 47.9 |
| 3 | A_u^1 | 70.8 | - | 66.1 | A_u^1 | 70.8 | 68.1 | - |
| 4 | A_g^1 | 74.8 | 70.3 | 78.4 | A_g^3 | 77.4 | 77.9 | 69.1 |
| 5 | E_u^1 | 83.3 | 80.5 | 81.1 | A_u^2 | 82.1 | 83.6 | 80.2 |
| 6 | E_u^1 | 83.3 | 80.5 | 82.6 | A_u^3 | 84.5 | 84.1 | 83.1 |
| 7 | A_g^2 | 86.6 | - | 87.2 | A_g^4 | 88.1 | 88.1 | - |
| 8 | E_g^2 | 91.1 | - | 88.9 | A_g^5 | 92.3 | 92.6 | - |
| 9 | E_g^2 | 91.1 | - | 93.5 | A_g^6 | 96.9 | 93.9 | - |
| 10 | E_g^3 | 98.9 | 96.4 | 95.4 | A_g^7 | 101.4 | 95.7 | 96.4 |
| 11 | E_g^3 | 98.9 | 96.4 | 100.5 | A_g^8 | 112.3 | 100.5 | 100.2 |
| 12 | E_u^2 | 114.3 | 108.9 | 110.3 | A_u^4 | 114.9 | 112.7 | 110.3 |
| 13 | E_u^2 | 114.3 | 108.9 | 111.4 | A_u^5 | 120.3 | 114.7 | 111.2 |

| | | | | | | | | |
|----|---------|-------|-------|-------|------------|-------|-------|-------|
| 14 | A_g^3 | 127.0 | 126.2 | 126.6 | A_g^9 | 130.0 | 128.4 | 127.4 |
| 15 | A_u^2 | 131.4 | - | 128.2 | A_u^6 | 132.4 | 130.4 | 131.7 |
| 16 | A_g^4 | 197.9 | - | 178.0 | A_g^{10} | 186.1 | 185.4 | - |
| 17 | E_u^3 | 226.4 | - | 216.8 | A_u^7 | 222.0 | 222.3 | - |
| 18 | E_u^3 | 226.4 | - | 220.2 | A_u^8 | 227.3 | 224.8 | - |
| 19 | E_g^4 | 232.8 | - | 225.4 | A_g^{11} | 231.2 | 227.2 | - |
| 20 | E_g^4 | 232.8 | - | 229.3 | A_g^{12} | 238.7 | 241.1 | - |
| 21 | A_u^3 | 255.0 | - | 244.1 | A_u^9 | 247.6 | 250.0 | 256.7 |

Figure 3 shows Raman spectra of bulk VI_3 measured in the back-scattering geometry at $T = 300$ K and 4 K. Four Raman active modes are identified at 300 K with frequencies of 48, 70, 96, and 126 cm^{-1} - see Figure 3a. The Raman intensities from the parallel (XX) and crossed (XY) polarization configuration spectra give us information about the symmetry of the Raman tensor for a given mode. The Raman intensity is proportional to $|\mathbf{e}_s^\dagger \mathbf{R} \mathbf{e}_i|^2$, where \mathbf{R} is the Raman polarizability tensor, and \mathbf{e}_s and \mathbf{e}_i are the polarization vectors of the scattered and incident light (off-resonant scattering)³³. By using this definition and the Raman tensors for the irreps of C_{3i} point group with the form:

$$R(A_g) = \begin{pmatrix} a & & \\ & a & \\ & & b \end{pmatrix} \quad (2)$$

$$R(^1E_g) = \begin{pmatrix} c & d & e \\ d & -c & f \\ e & f & \end{pmatrix} \quad (3)$$

$$R(^2E_g) = \begin{pmatrix} d & -c & -f \\ -c & -d & e \\ -f & e & \end{pmatrix} \quad (4)$$

we found two modes with A_g symmetry and two with E_g symmetry, similarly to the previous studies^{24,34}. The set of *gerade* phonon frequencies calculated for $R\bar{3}$ using the DFT that are given in Table 2 show very good agreement with the experimental results. We note that this result contradicts the Raman study of Djurdic et al.²⁴ claiming better agreement with the $P\bar{3}1c$ space group (D_{3d} point group) rather than with $R\bar{3}$.

The Raman spectrum at 4 K shown in Figure 3b corresponds to the triclinic FM phase (the phonons are labeled using C_i point group irreps) and contains three additional modes at 28.7, 76, and 160 cm^{-1} labeled as Ω_1 , Ω_2 , Ω_3 . A sharp Ω_1 and a broad Ω_3 resembles the modes observed below T_C by Lyu et al.¹⁹. They were ascribed to the zone-center acoustic magnon (two magnetic branches expected for two V atoms per unit cell) and two-magnon mode associated with the Van Hove singularity of the magnon density of states (DOS) corresponding presumably to the zone-boundary magnons. Besides, a small but clear splitting of the E_g^3 phonon into two modes A_g^7 and A_g^8 is present according to the opposite polarization selection rules.

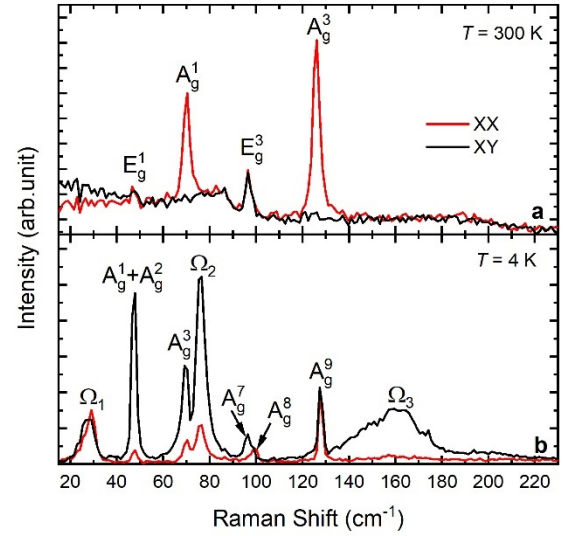


Figure 3: Polarization-resolved Raman spectra of VI_3 . **a**, taken at 300 K in the rhombohedral phase. **b**, taken at 4 K in the ferromagnetic triclinic phase. The Raman active phonons are named after the irreps of the given point group.

The temperature evolution of the Raman spectra from 300 K to 4 K is given in Figure 4a. No lifting of the E_g modes degeneracy is found at T_{S1} within the experimental energy resolution (~ 1 cm^{-1}), similarly to what was found for RuCl_3 ³⁵. Our DFT calculations show a relatively large splitting of the E_g^1 and E_g^3 modes ($\Delta\omega \sim 10$ cm^{-1} and ~ 20 cm^{-1}) when anti-dimerization is included while splitting due to dimerization is significantly smaller. On the other hand, this splitting is rather asymmetric and one of the peaks practically retains the position of its high symmetry parent. The intensity of the other component could be below the experimental sensitivity. Below T_C , two new features emerge in Raman spectra, a sharp Ω_2 mode accompanied by the formation of a broad Ω_3 , which develop and soften with further decreasing temperature. Below 35 K, an Ω_1 mode emerges just above our energy cut-off (12 cm^{-1}) and exhibits hardening with decreasing temperature down to 4 K. The hardening/softening trends of Ω_1 , Ω_2 and Ω_3 modes with decreasing temperature are much more significant compared to the Γ -point optical phonons. It is well documented in Figure 4b showing the temperature dependence of the frequencies of the Raman modes.

While the phonon frequency changes are within 3 cm^{-1} , the frequency shifts of Ω_1 , Ω_2 and Ω_3 approach 10, 11 and 18 cm^{-1} , respectively, in the temperature range between 45 K and 4 K (for Ω_1 between 25 K and 4 K). Such a strong temperature dependence of frequencies indicates that these three modes are connected with the evolution of magnetic structure⁹.

The Ω_1 and Ω_2 modes shift to higher frequencies with an increasing magnetic field, directly proving their magnetic origin. This aspect is presented here through the courtesy of Dr. M. Veis et al. as a result of their recent measurements of Raman spectra on VI_3 flakes (from the same batch as our samples) in the magnetic field³⁶. The evolution of Ω_1 with decreasing temperature qualitatively agrees with that observed for the acoustic magnon in¹⁹. This acoustic magnon originates from the out-of-plane magneto-crystalline anisotropy (MCA) creating a gap at the Γ -point in the magnon dispersion which is proportional to the MCA energy^{19, 37}. The assignment of the Ω_1 mode to a magnon is further supported by recent inelastic neutron scattering measurements that observed a Γ -point magnetic excitation with a gap of $\sim 4 \text{ meV}$ ($\sim 32 \text{ cm}^{-1}$) at 2 K³⁸, which almost coincides in frequency with Ω_1 ($\sim 29 \text{ cm}^{-1}$, $\sim 0.8 \text{ THz}$). Because of differences in frequency of Ω_1 obtained by different Raman experiments, we performed additional testing measurements on different samples, which revealed that the Ω_1 frequency may get lower, $\sim 20 - 25 \text{ cm}^{-1}$, and that this depends on the laser spot location in the sample (see Figure S6). These values are

closer to the acoustic magnon energy of $\sim 18.5 \text{ cm}^{-1}$ at 1.7 K reported in¹⁹. In any case, the observed ferromagnetic magnon mode Ω_1 is three orders of magnitude higher in energy than those observed in conventional ferromagnets³⁹.

As for the Ω_2 mode one may consider assigning it to an optical magnon originating from the upper branch in the Ω_1 magnon dispersion or to a second acoustic magnon. The existence of two acoustic magnon branches in VI_3 with two different gaps at the Γ -point was observed by inelastic neutron scattering³⁸ and explained by associating them with two coexisting VI_3 structure domains hosting different V^{3+} orbital ground states due to oppositely distorted octahedral V^{3+} environments. This picture is consistent with the two inequivalent V moment sites observed by NMR and supported by muon experiment⁴⁰, one of them with an ordered magnetic moment existing only below T_{S2} and the other up to T_C ⁶. The Ω_2 mode frequency at 4 K ($\sim 76 \text{ cm}^{-1}$) is, however, 26 % higher compared to the upper Γ -point magnetic excitation of $\sim 7 \text{ meV}$ ($\sim 56 \text{ cm}^{-1}$) seen by neutrons. The broad Ω_3 mode does not show any magnetic-field dependence¹⁹. Its large width of 27 cm^{-1} at 4 K indicates a second-order scattering⁴¹. The analogous temperature dependence of the frequencies of Ω_2 and Ω_3 , where the frequency of Ω_3 is roughly twice as high as that of Ω_2 (see Figure 4b), suggests that they might originate from the same branch.

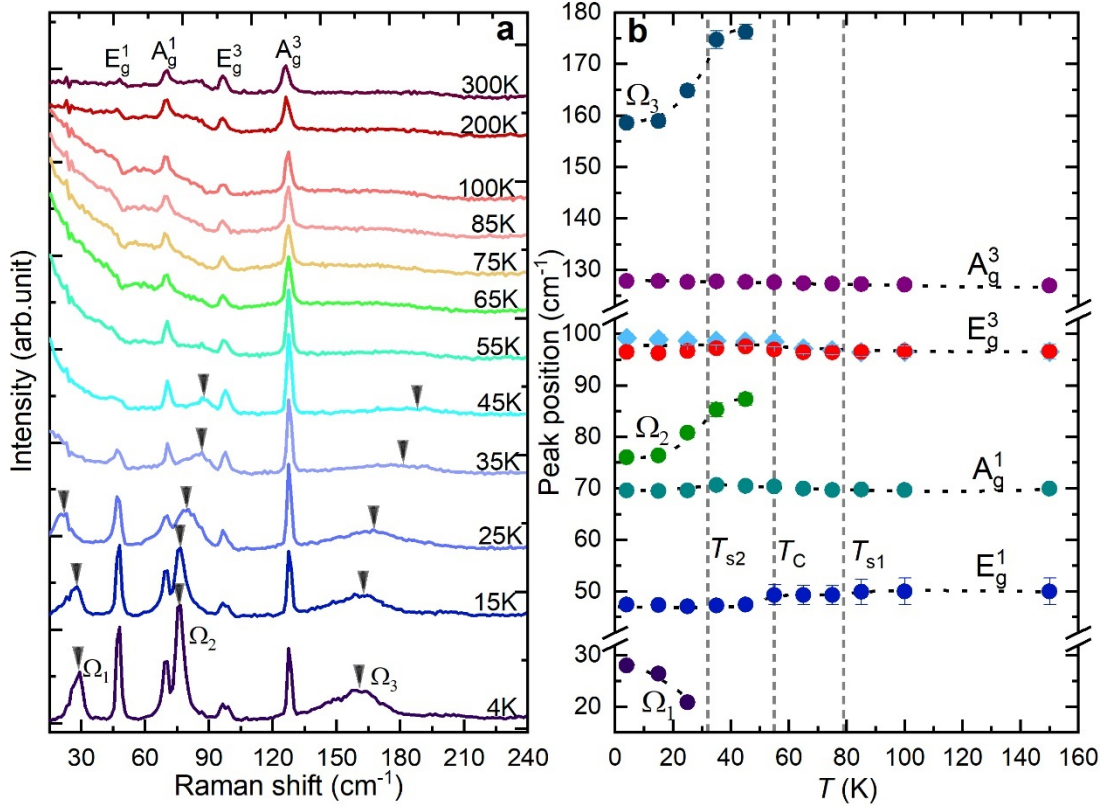


Figure 4: Temperature evolution of the unpolarized Raman spectra. **a**, temperature-dependent unpolarized Raman spectra taken from 300 K to 4 K in zero magnetic field. The Ω_1 mode emerges only below T_{S2} whereas Ω_2 and Ω_3 survive up to T_C , (marked by arrows). **b**, peaks positions in frequency as a function of temperature obtained from the spectra presented in **a**. For

E_g^3 mode the peak position measured in XX (blue diamonds) and XY (red circles) polarization configuration is given as the mode exhibits splitting under different polarization configurations. The peaks were fitted with the pseudo-Voigt function except for the E_g^1 mode where we used a Fano resonance shape function.

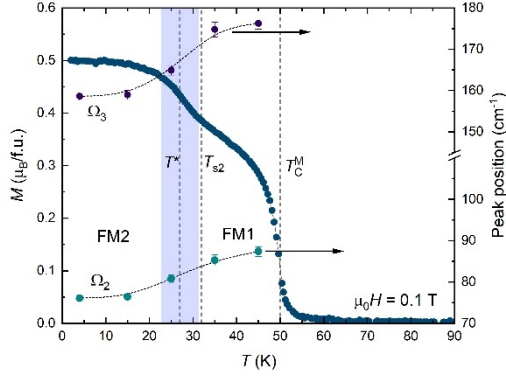


Figure 5: The temperature dependence of frequencies of Ω_2 and Ω_3 mode. The magnetization as a function of temperature measured after zero-field cooling with the magnetic field applied within the ab -plane is shown together with the temperature dependence of Ω_2 and Ω_3 mode's frequencies. The plot should emphasize the correlation of the Raman modes with the in-plane magnetic moment rotation happening around the temperature of the second structural transition.

To investigate the connection of Ω_2 and Ω_3 modes with magnetism, we compare the temperature dependence of frequencies of these two modes with the in-plane magnetization - see Figure 5. We note that both modes dramatically soften around T^* (just below T_{S2}) where the in-plane spin reorientation, causing a change of the magnetization, has been observed ⁹. This cross-correlation further supports that Ω_2 and Ω_3 are of magnetic origin.

Next, we analyze the temperature dependence of the polarization selection rules of different modes in the Raman spectra seen in Figure 6a. The Raman tensors for the monoclinic phase with the point group symmetry C_{2h} are derived as:

$$R(A_g) = \begin{pmatrix} a & c & d \\ d & c & b \end{pmatrix} \quad (5)$$

$$R(B_g) = \begin{pmatrix} e & f \\ e & f \end{pmatrix} \quad (6)$$

Since in our experimental setup (backscattering geometry with the polarization of the incident and scattered light parallel to the V honeycomb planes) we probe only the elements of the top left two-by-two submatrix of Equation (5), the A_g modes are forbidden in the XY channel below T_{S1} . This is consistent with our

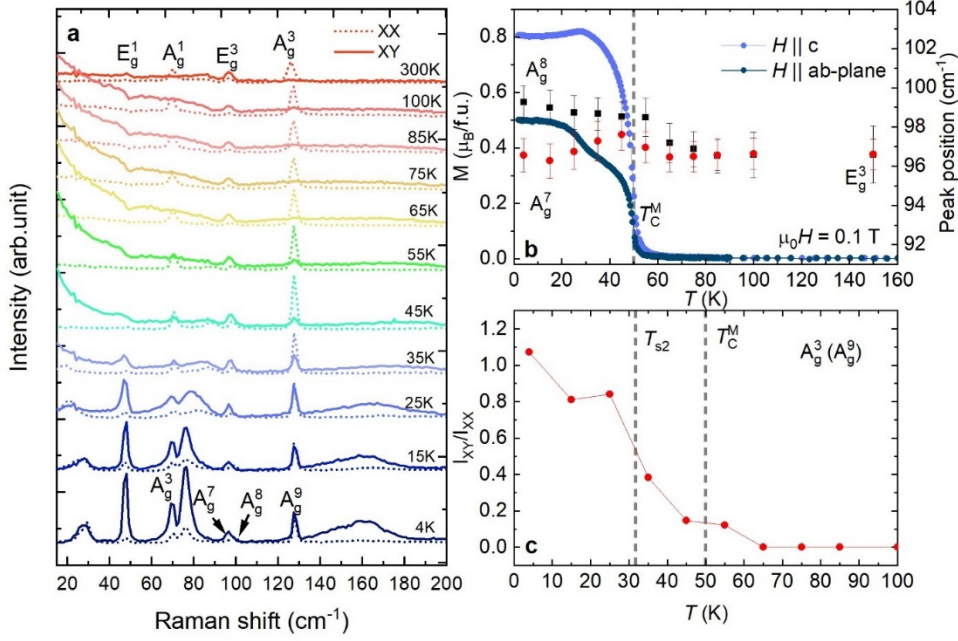


Figure 6: Temperature dependence of the Polarized Raman spectra. **a**, Polarized Raman spectra of bulk VI₃ as a function of temperature. **b**, The temperature dependence of the frequency of E_g³ phonon mode in XX (black squares) and XY (red circles) polarization configuration and magnetization of VI₃. **c**, The polarization intensity ratio I_{xy}/I_{xx} for A_g³ mode as a function of temperature.

results where the A_g³ (A_g¹ in rhombohedral phase) and the A_g⁹ (A_g³ in the monoclinic phase) modes remain silent in the XY polarization configuration. However, both modes start to appear in the XY channel at T ≈ 55 K. Such polarization change indicates a modification of selection rules due to the FM order breaking time-reversal symmetry which was also observed in CrI₃¹⁴. The temperature-dependent polarization intensity ratio I_{xy}/I_{xx} of the dominant A_g⁹ mode shown in Figure 6c demonstrate this effect. A relevant explanation can be obtained from the group theory analysis. Given the V³⁺ magnetic moment alignment above T_{S2}⁹, the magnetic point group of bulk VI₃ is likely C_{2h}(C_i) = {e, RC₂, i, Rσ_h}, where R is the time-reversal operator. In the FM state, the Raman tensor for the A_g optical phonon has the same form as that for the optical magnon because they have identical symmetry⁴². Therefore, the Raman tensor for the A_g mode given by the co-representation of the C_{2h}(C_i) magnetic point group^{14,43} has the form

$$R_{FM}(A_g) = \begin{pmatrix} a & ih & d \\ ig & c & ik \\ d & ij & b \end{pmatrix} \quad (7)$$

The imaginary off-diagonal terms in Equation (7) can explain the non-zero Raman scattering intensity in the XY polarization configuration present between T_C and T_{S2}.

A closer inspection of the Raman spectra in Figure 6a reveals the splitting of the E_g³ phonon mode as the peak position is slightly different under XX and XY polarization configurations. Experimentally, we observe almost no separation of the two modes (A_g⁷+A_g⁸) in the

paramagnetic phase measured in both polarization configurations. Nevertheless, in the FM phase, the vibrational frequencies shift oppositely with decreasing temperature as shown in Figure 6b. We tentatively attribute this effect to a MEC. A decrease of one phonon frequency on cooling below T_C indicates ferromagnetic interactions between ions involved in this phonon vector^{44,45} as was observed in NiPS₃¹⁸. Higher-resolution Raman spectroscopy is, however, necessary to accurately determine the mode-splitting temperature.

It is worth making a few remarks about the polarization properties of the Ω₁ magnon. The well-known theory of Fleury and London⁴¹ predicts the purely antisymmetric (present only in the XY configuration) Raman scattering from the first-order magnetic excitation regardless of crystal orientation. This theoretical prediction successfully explains a variety of ferromagnetic and antiferromagnetic materials with Raman active magnons^{41,46,47}. However, the theory uses the approximation of a zero or quenched angular momentum ground state L = 0⁴¹ which appears not to be true for VI₃^{12,48}. The recent work of McCreary et al.⁴⁹ on vdW FePS₃ pointed out the deviation from the purely antisymmetric response of a magnon and ascribed it to the non-zero L. In our case, we observe the Ω₁ magnon in both XX and XY polarization configurations which is in stark contrast with the Fleury and London theory. This anomaly further corroborates the suggested picture of a high orbital momentum on V³⁺ ion^{12,48,50}.

Furthermore, we notice a large contribution from the quasi-elastic scattering (QES) centered around the Rayleigh line which is present mainly in the XY polarization configuration shown in Figure 6a. The QES

is usually detected in highly frustrated and low-dimensional magnetic systems. The fluctuations of magnetic energy density are believed to be the source of this phenomenon^{16, 35, 51, 52}. Since the VI_3 has low frustration index⁵³, we attribute this effect to the quasi-2D nature of the magnetism. The intensity of the QES increases upon cooling and reaches its maximum at around 80 K and 65 K for the XX and XY polarization configurations, respectively. Then it steadily decreases turning into the Ω_1 acoustic magnon at around 35 K. Following the theory of Riter⁵⁴ and Halley⁵⁵ the Raman response for Stokes scattering defined as $\chi''(\omega) = I(\omega)/[n(\omega) - 1]$ where $n(\omega)$ is the Bose-Einstein factor, is given as^{56, 57}

$$\frac{\chi''(\omega)}{\omega} \propto C_m T \frac{Dk^2}{\omega^2 + (Dk^2)^2} \quad (8)$$

where C_m is magnetic specific heat and D is thermal diffusion constant. To obtain the spectral weight of QES we fit the normalized Raman response $\chi''(\omega)/\omega$ data with a Lorentzian function and integrate within the frequency range of 12-100 cm^{-1} (see Figure S7). The temperature dependence of the spectral weight of QES for both XX and XY polarization configurations is given in Figure 7a. We can note that the QES spectral weight peaks around T_{S1} for XX polarization configuration, whereas for XY the dominant peak shows its maximum around 65 K. These results provide microscopic evidence of the presence of FM fluctuations as a precursor of long-range FM order, far above T_C in the paramagnetic state. Interestingly, the FM fluctuations survive even below T_C as displayed by the non-negligible QES spectral weight contribution probably coming from the still fluctuating V moment.

Another interesting feature we notice is the temperature evolution of the prominent spectral line shape of the E_g^1 (corresponds to $A_g^1 + A_g^2$ below T_{S1}) phonon mode. As Figure 4a and 6a show, this mode exhibits clear characteristics of a Fano resonance; slight asymmetry at high temperatures followed by the mode appearing as a dip in the spectrum superposed on QES which turns into an asymmetric peak at around 55 K, and finally, the asymmetry vanishes at the low-temperature limit. The Fano resonance requires quantum interference between a discrete excitation and a continuum⁵⁸ and the resonance line shape is described by the form

$$I(\omega) = I_0 \frac{[1 + (\omega - \omega_0)/q\Gamma]^2}{1 + [(\omega - \omega_0)/\Gamma]^2} \quad (9)$$

where ω_0 and Γ are the bare frequency and width of the phonon, and q is the asymmetry parameter, where $1/|q|$ correlates with the strength of the coupling. In this case, the discrete excitation and the continuum correspond to the E_g^1 phonon and magnetic continuum states, respectively. Therefore, the $1/|q|$ parameter is proportional to the spin-phonon coupling strength⁵⁹. With the subtraction of the QES we fitted the E_g^1 phonon

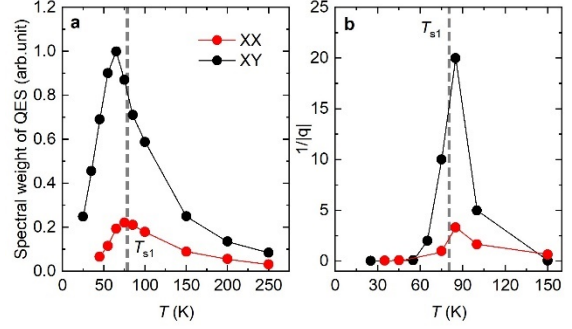


Figure 7: Temperature dependence of the Spectral weight of the QES and the Fano asymmetry parameter. **a**, the integrated intensities of the QES plotted as a function of temperature for both polarization configuration. Both dependences show maximum around the temperature of the first structural transition T_{S1} (~ 80 K and 65 K for XX and XY channel, respectively). **b**, the inverse Fano asymmetry parameter for E_g^1 phonon mode as a function of temperature for both polarization configurations peaks at around T_{S1} which indicates strong coupling between the phonon mode and the magnetic continuum.

with Equation (9) (see Figure S8) with the $1/|q|$ plotted in Figure 7b. The $1/|q|$ parameter shows a maximum in the temperature range of the first structural transition where the QES is relatively strong and the spectral weight of QES spans a wide frequency range. This suggests a tight coupling between the phonon mode and the FM fluctuations which results in the anti-resonance. Interestingly, the striking magnetic field dependence of the structural transition at T_{S1} observed by Dolezal et al.⁷ could be potentially connected to this effect. At the low-temperature limit, where the QES is significantly suppressed by FM order, we observe a negligible value of $1/|q|$, which is a characteristic of regular resonance dominated by phonon scattering. We note, that a similar evolution of the E_g^1 phonon mode with temperature was reported for VI_3 thin films¹⁹.

In summary, we have studied the lattice and magnetic properties of single crystals of the vdW compound VI_3 at temperatures down to 4 K by combining infrared, terahertz, and Raman spectroscopy and employing relevant DFT calculations of phonon modes. The observed results confirm and complement the state of understanding of the evolution of crystal structure and magnetic phases with varying temperatures. The IR and THz spectra revealed splitting of phonon modes upon cooling of the crystal through the structural transition at T_{S1} which confirms the symmetry lowering due to the change of the trigonal phase to monoclinic. In addition, the large enhancement of the QES between T_{S1} and T_C detected by the Raman scattering reflects the presence of strong FM fluctuations at temperatures far above T_C which are tightly coupled to at least one phonon mode. The onset of the long-range FM order is apparent from observed variations of phonon frequencies at T_C via MEC enhanced by strong spin-orbit interaction. Moreover, the modification of the Raman polarization selection rules for optical phonons at T_C unambiguously demonstrates

that Raman spectroscopy can be used as a simple probe of magnetic phases for VI_3 and potentially for other vdW compounds.

The Raman spectra revealed a high-frequency acoustic magnon in the THz range emerging below the critical temperature T_{S2} of the second structural transition accompanied by order-order magnetic phase transition. In addition, two new Raman active modes are observed below T_C . They show a dramatic softening in the narrow temperature interval around T_{S2} in which the order-order magnetic phase transition involving rotation of in-plane magnetic moment has been reported⁹. The THz range of magnon frequency in VI_3 is three orders of magnitude higher than typical GHz magnon frequencies in conventional ferromagnets. This suggests that some 2D van der Waals ferromagnets can be useful in ultrafast THz spintronic applications, which were believed to be exclusively the domain of antiferromagnets.

Methods

Sample Fabrication. The VI_3 single crystals have been grown through the chemical vapor transport method directly from a stoichiometric (1:3) ratio of 2N5 purity V powder (Goodfellow) and 5N ultra dried I_2 lumps (ThermoFisher) in a quartz ampoule evacuated down to 10^{-7} bar. Preparation of elements as well as the filing of the quartz ampoule was performed in a glove box under Ar inert atmosphere. The growth process was realized in a two-zone gradient furnace. Two processes were tested. In the first case, the procedure reported by Tian et al.⁵ was followed. The starting material was gradually heated up to 650°C for 4 days. Then a gradient of $650/550^\circ\text{C}$ was kept for 8 days. All material was transported and tens of micrometers thick single crystals of several millimeters of lateral size were obtained, however, rather unstable in the air avoiding almost any operation outside of the glovebox. The degradation process of these crystals was described in detail by Kratochvilova et al.³².

In the second procedure, the work of Son et al. [3] was reproduced. First, the material was gradually heated up to 400°C for four days and then a gradient of $400/320^\circ\text{C}$ was kept for 2 weeks. The process was significantly slower than the first one, approximately half of the input material remained untransported in the cold part. Nevertheless, we have obtained very large single crystals (several of them exceeding 0.5 cm^2) of a very reflective surface. Single crystals prepared by this procedure are much more stable in the air, for 2 hours without any surface degradation effect. Traces of degradation began to appear only locally in places where the single crystal was mechanically deformed, however, the degradation remained on the surface and provoked a negligible bulk effect after 5 hours. The chemical composition of single crystals was verified by scanning electron microscopy (SEM) using a Tescan Mira I LMH system equipped with an energy-dispersive X-ray detector (EDX) Bruker AXS. The EDX analysis revealed a single-phase single crystal of the stoichiometric VI_3 composition.

Optical Experiments. For Raman studies of single crystals, a Renishaw RM1000 Micro-Raman

spectrometer with Bragg filters was used, equipped with an Oxford Instruments Microstat continuous flow optical He cryostat. The measurements were performed using an Ar^+ ion laser operating at 514.5 nm in the backscattering geometry. Low-temperature infrared (IR) transmittance measurements in the frequency range $20 - 660\text{ cm}^{-1}$ (0.6-20 THz) were performed using a Bruker IFS-113v Fourier-transform IR spectrometer equipped with a liquid-He-cooled Si bolometer (1.6 K) serving as a detector. For the low-temperature IR and THz spectroscopies, continuous-He-flow cryostats (Optistat, Oxford Instruments) with polyethylene and mylar windows, respectively, were used. Temperature-dependent THz spectra of complex transmittance between 0.5 and 3 THz ($16\text{-}100\text{ cm}^{-1}$) were obtained using a custom-made time-domain spectrometer utilizing a Ti: sapphire femtosecond oscillator⁶⁰.

Theoretical calculations. Phonon dynamical matrix elements were calculated self-consistently using density functional theory (DFT) calculations in the band structure program ELK⁶¹ for each phonon wave vector k inside a supercell commensurate with k . These calculations employed the full-potential linear augmented plane wave (FP-LAPW) method combined with the generalized gradient approximation (GGA) parametrized by Perdew-Burke-Ernzerhof⁶². This exchange-correlation functional represents an appropriate choice for phonon studies. Spin-orbit coupling (SOC) is known to play a key role in this system^{12,48} and has been included in the calculation. Hubbard U allows us to describe approximately the strong electron correlations present in the system and form the correct band gap in the calculated electronic structure, while standard LDA calculation would lead to a metallic solution. Our calculations have used $U = 3.8\text{ eV}$ added to the Hamiltonian within the fully localized limit double counting treatment⁶³ and a band gap of size around 0.6 eV is predicted. The full Brillouin zone has been sampled by about 800 k -points. Increased accuracy of expansion into spherical harmonics has been used with $l_{\text{max}} = 14$

ACKNOWLEDGMENT

This work is a part of the research project GAČR 21-06083S which is financed by the Czech Science Foundation. The work of D.R. was supported by the Grant Agency of the Czech Technical University in Prague (Project No. SGS22/182/OHK4/3T/14). The VI_3 single crystals have been grown and characterized in the Materials Growth and Measurement Laboratory MGML (see: <http://mgml.eu>) which is supported by the program of Czech Research Infrastructures (project no. LM2018096). This work was also supported by the Grant No. CZ.02.1.01/0.0/0.0/15_003/0000487 (OP VVV project MATFUN). The authors are indebted to Dr. Martin Veis for kindly providing information on Raman data recorded on VI_3 in the magnetic field. The authors are indebted to Dr. Ross Colman for critical reading and correcting the manuscript.

REFERENCES

- (1) McGuire, M. A. Crystal and Magnetic Structures in Layered, Transition Metal Dihalides and Trihalides. *Crystals* **2017**, *7* (5), 121.
- (2) McGuire, M. A.; Dixit, H.; Cooper, V. R.; Sales, B. C. Coupling of Crystal Structure and Magnetism in the Layered, Ferromagnetic Insulator CrI₃. *Chemistry of Materials* **2015**, *27* (2), 612-620. DOI: 10.1021/cm504242t.
- (3) Son, S.; Coak, M. J.; Lee, N.; Kim, J.; Kim, T. Y.; Hamidov, H.; Cho, H.; Liu, C.; Jarvis, D. M.; Brown, P. A. C.; et al. Bulk properties of the van der Waals hard ferromagnet VI₃. *Physical Review B* **2019**, *99* (4), 041402. DOI: 10.1103/PhysRevB.99.041402.
- (4) Kong, T.; Stolze, K.; Timmons, E. I.; Tao, J.; Ni, D.; Guo, S.; Yang, Z.; Prozorov, R.; Cava, R. J. VI₃—a New Layered Ferromagnetic Semiconductor. *Advanced Materials* **2019**, *31* (17), 1808074. DOI: <https://doi.org/10.1002/adma.201808074>.
- (5) Tian, S.; Zhang, J.-F.; Li, C.; Ying, T.; Li, S.; Zhang, X.; Liu, K.; Lei, H. Ferromagnetic van der Waals Crystal VI₃. *Journal of the American Chemical Society* **2019**, *141* (13), 5326-5333. DOI: 10.1021/jacs.8b13584.
- (6) Gati, E.; Inagaki, Y.; Kong, T.; Cava, R. J.; Furukawa, Y.; Canfield, P. C.; Bud'ko, S. L. Multiple ferromagnetic transitions and structural distortion in the van der Waals ferromagnet VI₃ at ambient and finite pressures. *Physical Review B* **2019**, *100* (9), 094408. DOI: 10.1103/PhysRevB.100.094408.
- (7) Doležal, P.; Kratochvílová, M.; Holý, V.; Čermák, P.; Sechovský, V.; Dušek, M.; Míšek, M.; Chakraborty, T.; Noda, Y.; Son, S.; et al. Crystal structures and phase transitions of the van der Waals ferromagnet VI₃. *Physical Review Materials* **2019**, *3* (12), 121401. DOI: 10.1103/PhysRevMaterials.3.121401.
- (8) Marchandier, T.; Dubouis, N.; Fauth, F.; Avdeev, M.; Grimaud, A.; Tarascon, J.-M.; Rouse, G. Crystallographic and magnetic structures of the VI₃ and LiVI₃ van der Waals compounds. *Physical Review B* **2021**, *104* (1), 014105. DOI: 10.1103/PhysRevB.104.014105.
- (9) Hao, Y.; Gu, Y.; Gu, Y.; Feng, E.; Cao, H.; Chi, S.; Wu, H.; Zhao, J. Magnetic Order and Its Interplay with Structure Phase Transition in van der Waals Ferromagnet VI₃. *Chinese Physics Letters* **2021**, *38*, 096101. DOI: 10.1088/0256-307x/38/9/096101.
- (10) Yan, J.; Luo, X.; Chen, F. C.; Gao, J. J.; Jiang, Z. Z.; Zhao, G. C.; Sun, Y.; Lv, H. Y.; Tian, S. J.; Yin, Q. W.; et al. Anisotropic magnetic entropy change in the hard ferromagnetic semiconductor VI₃. *Physical Review B* **2019**, *100* (9), 094402. DOI: 10.1103/PhysRevB.100.094402.
- (11) Koriki, A.; Míšek, M.; Pospíšil, J.; Kratochvílová, M.; Carva, K.; Prokleška, J.; Doležal, P.; Kaštil, J.; Son, S.; Park, J. G.; et al. Magnetic anisotropy in the van der Waals ferromagnet VI₃. *Physical Review B* **2021**, *103* (17), 174401. DOI: 10.1103/PhysRevB.103.174401.
- (12) Sandratskii, L. M.; Carva, K. Interplay of spin magnetism, orbital magnetism, and atomic structure in layered van der Waals ferromagnet VI₃. *Physical Review B* **2021**, *103* (21), 214451. DOI: 10.1103/PhysRevB.103.214451.
- (13) Kim, K.; Lee, J. U.; Cheong, H. Raman spectroscopy of two-dimensional magnetic van der Waals materials. *Nanotechnology* **2019**, *30* (45), 10, Review. DOI: 10.1088/1361-6528/ab37a4.
- (14) Zhang, Y.; Wu, X.; Lyu, B.; Wu, M.; Zhao, S.; Chen, J.; Jia, M.; Zhang, C.; Wang, L.; Wang, X.; et al. Magnetic Order-Induced Polarization Anomaly of Raman Scattering in 2D Magnet CrI₃. *Nano Letters* **2020**, *20* (1), 729-734. DOI: 10.1021/acs.nanolett.9b04634.
- (15) Lei, M.; Coh, S. Large cross-polarized Raman signal in CrI₃: A first-principles study. *Physical Review Materials* **2021**, *5* (2), 025202. DOI: 10.1103/PhysRevMaterials.5.025202.
- (16) Tian, Y.; Gray, M. J.; Ji, H.; Cava, R. J.; Burch, K. S. Magneto-elastic coupling in a potential ferromagnetic 2D atomic crystal. *2D Materials* **2016**, *3* (2), 025035. DOI: 10.1088/2053-1583/3/2/025035.
- (17) Milosavljević, A.; Šolajić, A.; Djurdjić-Mijin, S.; Pešić, J.; Višić, B.; Liu, Y.; Petrovic, C.; Lazarević, N.; Popović, Z. V. Lattice dynamics and phase transitions in Fe_{3-x}GeTe₂. *Physical Review B* **2019**, *99* (21), 214304. DOI: 10.1103/PhysRevB.99.214304.

- (18) Kim, K.; Lim, S. Y.; Lee, J.-U.; Lee, S.; Kim, T. Y.; Park, K.; Jeon, G. S.; Park, C.-H.; Park, J.-G.; Cheong, H. Suppression of magnetic ordering in XXZ-type antiferromagnetic monolayer NiPS₃. *Nature Communications* **2019**, *10* (1), 345. DOI: 10.1038/s41467-018-08284-6.
- (19) Lyu, B.; Gao, Y.; Zhang, Y.; Wang, L.; Wu, X.; Chen, Y.; Zhang, J.; Li, G.; Huang, Q.; Zhang, N.; et al. Probing the Ferromagnetism and Spin Wave Gap in VI₃ by Helicity-Resolved Raman Spectroscopy. *Nano Letters* **2020**, *20* (8), 6024-6031. DOI: 10.1021/acs.nanolett.0c02029.
- (20) Vaclavkova, D.; Palit, M.; Wyzula, J.; Ghosh, S.; Delhomme, A.; Maity, S.; Kapuscinski, P.; Ghosh, A.; Veis, M.; Grzeszczyk, M.; et al. Magnon polarons in the van der Waals antiferromagnet FePS₃. *Physical Review B* **2021**, *104* (13), 134437. DOI: 10.1103/PhysRevB.104.134437.
- (21) YU, P.; Cardona, M. *Fundamentals of Semiconductors: Physics and Materials Properties*; Springer Berlin Heidelberg, 2010.
- (22) Caldwell, J. D.; Lindsay, L.; Giannini, V.; Vurgafman, I.; Reinecke, T. L.; Maier, S. A.; Glembocki, O. J. Low-loss, infrared and terahertz nanophotonics using surface phonon polaritons. *Nanophotonics* **2015**, *4* (1), 44-68. DOI: doi:10.1515/nanoph-2014-0003 (accessed 2022-08-31).
- (23) Liu, Y.; Abeykoon, M.; Petrovic, C. Critical behavior and magnetocaloric effect in VI₃. *Physical Review Research* **2020**, *2* (1), 013013. DOI: 10.1103/physrevresearch.2.013013.
- (24) Djurdjic Mijin, S.; Abeykoon, A. M. M.; Šolajić, A.; Milosavljević, A.; Pešić, J.; Liu, Y.; Petrovic, C.; Popović, Z. V.; Lazarević, N. Short-Range Order in VI₃. *Inorganic Chemistry* **2020**, *59* (22), 16265-16271. DOI: 10.1021/acs.inorgchem.0c02060.
- (25) Aroyo, M. I.; Kirov, A.; Capillas, C.; Perez-Mato, J. M.; Wondratschek, H. Bilbao Crystallographic Server. II. Representations of crystallographic point groups and space groups. *Acta Crystallographica Section A* **2006**, *62* (2), 115-128. DOI: doi:10.1107/S0108767305040286.
- (26) Larson, D. T.; Kaxiras, E. Raman spectrum of CrI₃: An *ab initio* study. *Physical Review B* **2018**, *98* (8), 085406. DOI: 10.1103/PhysRevB.98.085406.
- (27) Lin, J.; Miller, G. J. Dimensional diversity in transition metal trihalides. *Inorganic Chemistry* **1993**, *32* (8), 1476-1487.
- (28) Petzelt, J.; Dvorak, V. Changes of infrared and Raman spectra induced by structural phase transitions. I. General considerations. *Journal of Physics C: Solid State Physics* **1976**, *9* (8), 1571-1586. DOI: 10.1088/0022-3719/9/8/028.
- (29) Soler-Delgado, D.; al., e. Probing magnetism in exfoliated VI₃ layers with magnetotransport. <https://dx.doi.org/10.48550/arxiv.2204.10010> **2022**. DOI: 10.48550/arxiv.2204.10010.
- (30) Lin, Z.; Huang, B.; Hwangbo, K.; Jiang, Q.; Zhang, Q.; Liu, Z.; Fei, Z.; Lv, H.; Millis, A.; McGuire, M.; et al. Magnetism and Its Structural Coupling Effects in 2D Ising Ferromagnetic Insulator VI₃. *Nano Letters* **2021**, *21* (21), 9180-9186. DOI: 10.1021/acs.nanolett.1c03027.
- (31) Valenta, J.; Kratochvílová, M.; Míšek, M.; Carva, K.; Kaštil, J.; Doležal, P.; Opletal, P.; Čermák, P.; Proschek, P.; Uhlířová, K.; et al. Pressure-induced large increase of Curie temperature of the van der Waals ferromagnet VI₃. *Physical Review B* **2021**, *103* (5), 054424. DOI: 10.1103/PhysRevB.103.054424.
- (32) Kratochvílová, M.; Uhlířová, K.; Míšek, M.; Holý, V.; Zázvorka, J.; Veis, M.; Pospíšil, J.; Son, S.; Park, J. G.; Sechovský, V. The surface degradation and its impact on the magnetic properties of bulk VI₃. *Materials Chemistry and Physics* **2022**, *278*, 125590. DOI: <https://doi.org/10.1016/j.matchemphys.2021.125590>.
- (33) Loudon, R. The Raman effect in crystals. *Advances in Physics* **1964**, *13* (52), 423-482. DOI: 10.1080/00018736400101051.
- (34) Wang, Y.-M.; Tian, S.-J.; Li, C.-H.; Jin, F.; Ji, J.-T.; Lei, H.-C.; Zhang, Q.-M. Raman scattering study of two-dimensional magnetic van der Waals compound VI₃. *Chinese Physics B* **2020**, *29* (5), 056301. DOI: 10.1088/1674-1056/ab8215.
- (35) Li, G.; Chen, X.; Gan, Y.; Li, F.; Yan, M.; Ye, F.; Pei, S.; Zhang, Y.; Wang, L.; Su, H.; et al. Raman spectroscopy evidence for dimerization and Mott collapse in α -RuCl₃ under pressures. *Physical Review Materials* **2019**, *3* (2), 023601. DOI: 10.1103/PhysRevMaterials.3.023601.
- (36) PRIVATE COMUNACTIONS, Dr. Martin Veis et al. (private communications). **2022**.
- (37) Jin, W.; Kim, H. H.; Ye, Z.; Li, S.; Rezaie, P.; Diaz, F.; Siddiq, S.; Wauer, E.; Yang, B.; Li, C.; et

- al. Raman fingerprint of two terahertz spin wave branches in a two-dimensional honeycomb Ising ferromagnet. *Nature Communications* **2018**, *9* (1), 5122. DOI: 10.1038/s41467-018-07547-6.
- (38) Lane, H.; Pachoud, E.; Rodriguez-Rivera, J. A.; Songvilay, M.; Xu, G.; Gehring, P. M.; Attfield, J. P.; Ewings, R. A.; Stock, C. Two-dimensional ferromagnetic spin-orbital excitations in honeycomb VI_3 . *Physical Review B* **2021**, *104* (2), L020411. DOI: 10.1103/PhysRevB.104.L020411.
- (39) Walowski, J.; Münzenberg, M. Perspective: Ultrafast magnetism and THz spintronics. *Journal of Applied Physics* **2016**, *120* (14), 140901. DOI: 10.1063/1.4958846.
- (40) Wang, Q. H.; Bedoya-Pinto, A.; Blei, M.; Dismukes, A. H.; Hamo, A.; Jenkins, S.; Koperski, M.; Liu, Y.; Sun, Q.-C.; Telford, E. J.; et al. The Magnetic Genome of Two-Dimensional van der Waals Materials. *ACS Nano* **2022**, *16* (5), 6960-7079. DOI: 10.1021/acsnano.1c09150.
- (41) Fleury, P. A.; Loudon, R. Scattering of Light by One- and Two-Magnon Excitations. *Physical Review* **1968**, *166* (2), 514-530. DOI: 10.1103/PhysRev.166.514.
- (42) Anastassakis, E.; Burstein, E. Morphic effects. V. Time reversal symmetry and the mode properties of long wavelength optical phonons. *Journal of Physics C: Solid State Physics* **1972**, *5* (17), 2468-2481. DOI: 10.1088/0022-3719/5/17/021.
- (43) Cracknell, A. P. Scattering matrices for the Raman effect in magnetic crystals. *Journal of Physics C: Solid State Physics* **1969**, *2* (3), 500-511. DOI: 10.1088/0022-3719/2/3/314.
- (44) Wakamura, K.; Arai, T. Effect of magnetic ordering on phonon parameters for infrared active modes in ferromagnetic spinel CdCr_2S_4 . *Journal of Applied Physics* **1988**, *63* (12), 5824-5829. DOI: 10.1063/1.340321.
- (45) Baltensperger, W.; Helman, J. S. Influence of magnetic order in insulators on the optical phonon frequency. *Helvetica Physica Acta* **1968**, *41*, 668-673. DOI: 10.5169/seals-113910.
- (46) Koshizuka, N.; Hayashi, K. Raman Scattering from Magnon Excitations in RFeO_3 . *Journal of the Physical Society of Japan* **1988**, *57* (12), 4418-4428. DOI: 10.1143/JPSJ.57.4418 (accessed 2022/07/13).
- (47) Venugopalan, S.; Petrou, A.; Galazka, R. R.; Ramdas, A. K.; Rodriguez, S. Raman scattering by phonons and magnons in semimagnetic semiconductors: $\text{Cd}_{1-x}\text{Mn}_x\text{Te}$. *Physical Review B* **1982**, *25* (4), 2681-2696. DOI: 10.1103/PhysRevB.25.2681.
- (48) Yang, K.; Fan, F.; Wang, H.; Khomskii, D. I.; Wu, H. VI_3 : A two-dimensional Ising ferromagnet. *Physical Review B* **2020**, *101* (10), 100402. DOI: 10.1103/PhysRevB.101.100402.
- (49) McCreary, A.; Simpson, J. R.; Mai, T. T.; McMichael, R. D.; Douglas, J. E.; Butch, N.; Dennis, C.; Valdés Aguilar, R.; Hight Walker, A. R. Quasi-two-dimensional magnon identification in antiferromagnetic FePS_3 via magneto-Raman spectroscopy. *Physical Review B* **2020**, *101* (6), 064416. DOI: 10.1103/PhysRevB.101.064416.
- (50) Zhao, G.-D.; Liu, X.; Hu, T.; Jia, F.; Cui, Y.; Wu, W.; Whangbo, M.-H.; Ren, W. Difference in magnetic anisotropy of the ferromagnetic monolayers VI_3 and CrI_3 . *Physical Review B* **2021**, *103* (1), 014438. DOI: 10.1103/PhysRevB.103.014438.
- (51) Sandilands, L. J.; Tian, Y.; Plumb, K. W.; Kim, Y.-J.; Burch, K. S. Scattering Continuum and Possible Fractionalized Excitations in $\alpha\text{-RuCl}_3$. *Physical Review Letters* **2015**, *114* (14), 147201. DOI: 10.1103/PhysRevLett.114.147201.
- (52) Lemmens, P.; Güntherodt, G.; Gros, C. Magnetic light scattering in low-dimensional quantum spin systems. *Physics Reports* **2003**, *375* (1), 1-103. DOI: [https://doi.org/10.1016/S0370-1573\(02\)00321-6](https://doi.org/10.1016/S0370-1573(02)00321-6).
- (53) Ramirez, A. P. Strongly Geometrically Frustrated Magnets. *Annual Review of Materials Science* **1994**, *24* (1), 453-480. DOI: 10.1146/annurev.ms.24.080194.002321.
- (54) Reiter, G. F. Light scattering from energy fluctuations in magnetic insulators. *Physical Review B* **1976**, *13* (1), 169-173. DOI: 10.1103/PhysRevB.13.169.
- (55) Halley, J. W. Light Scattering as a Probe of Dynamical Critical Properties of Antiferromagnets. *Physical Review Letters* **1978**, *41* (23), 1605-1608. DOI: 10.1103/PhysRevLett.41.1605.
- (56) Glamazda, A.; Lemmens, P.; Do, S. H.; Choi, Y. S.; Choi, K. Y. Raman spectroscopic signature of fractionalized excitations in the harmonic-honeycomb iridates β - and $\gamma\text{-Li}_2\text{IrO}_3$. *Nature Communications* **2016**, *7* (1), 12286. DOI: 10.1038/ncomms12286.

- (57) Choi, K. Y.; Lemmens, P.; Berger, H. Critical spin dynamics of the $S=1/2$ spin chain compound CuSe_2O_5 . *Physical Review B* **2011**, *83* (17), 174413. DOI: 10.1103/PhysRevB.83.174413.
- (58) Fano, U. Effects of Configuration Interaction on Intensities and Phase Shifts. *Physical Review* **1961**, *124* (6), 1866-1878. DOI: 10.1103/PhysRev.124.1866.
- (59) Li, Z.; Lui, C. H.; Cappelluti, E.; Benfatto, L.; Mak, K. F.; Carr, G. L.; Shan, J.; Heinz, T. F. Structure-Dependent Fano Resonances in the Infrared Spectra of Phonons in Few-Layer Graphene. *Physical Review Letters* **2012**, *108* (15), 156801. DOI: 10.1103/PhysRevLett.108.156801.
- (60) Kužel, P.; Němec, H.; Kadlec, F.; Kadlec, C. Gouy shift correction for highly accurate refractive index retrieval in time-domain terahertz spectroscopy. *Opt. Express* **2010**, *18* (15), 15338-15348. DOI: 10.1364/OE.18.015338.
- (61) *The Elk Code*, <https://elk.sourceforge.io/>. url: <http://elk.sourceforge.net/>. (accessed 2022 02/10/2022).
- (62) Perdew, J. P.; Burke, K.; Ernzerhof, M. Generalized Gradient Approximation Made Simple *Physical Review Letters* **1997**, *78* (7), 1396-1396. DOI: 10.1103/PhysRevLett.78.1396.
- (63) Anisimov, V. I.; Zaanen, J.; Andersen, O. K. Band theory and Mott insulators: Hubbard U instead of Stoner I. *Physical Review B* **1991**, *44* (3), 943-954. DOI: 10.1103/PhysRevB.44.943.

Supplementary Information for

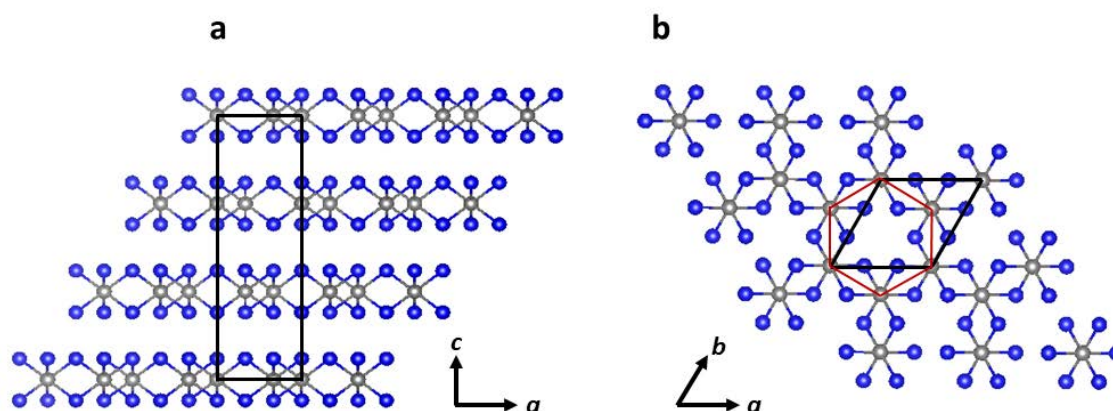


Figure S1| The crystal structure of the VI_3 at room temperature. **a**, a-c plane projection of four V-I triple-layers. **b**, a-b plane projection of one V-I triple-layer. In silver color V atoms, in blue color Iodine atoms. The chosen hexagonal unit cell corresponds to work¹ where we shifted the unit cell along the c -axis and set the V atom to $(0,0,0)$ position. The red hexagon emphasizes the in-plane honeycomb arrangement of V atoms.

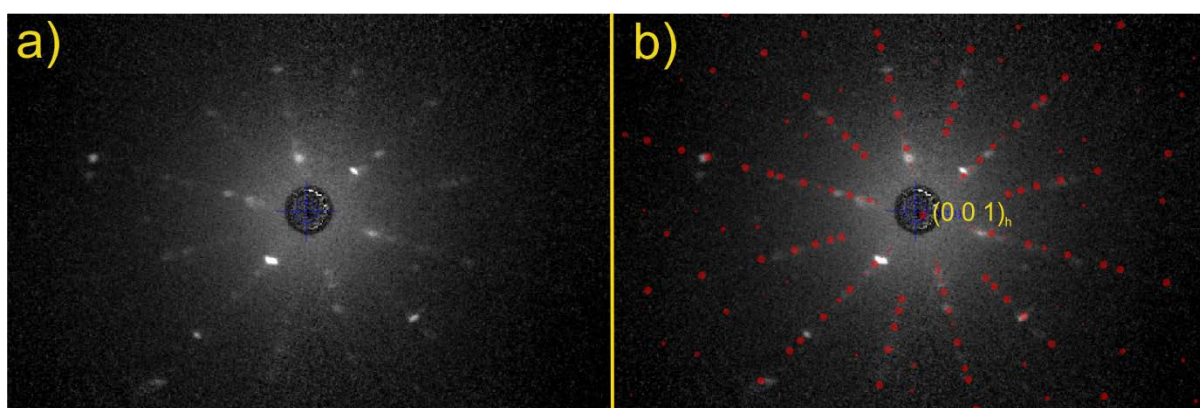


Figure S2| Laue image of VI_3 single crystal. **a**) bare image **b**) Comparison of measured pattern with the simulated one based on rhombohedral crystal structure model in work¹. The Laue

diffraction was performed on VI3 sample placed on a glass bar and covered by blue tape to slow down the degradation process.

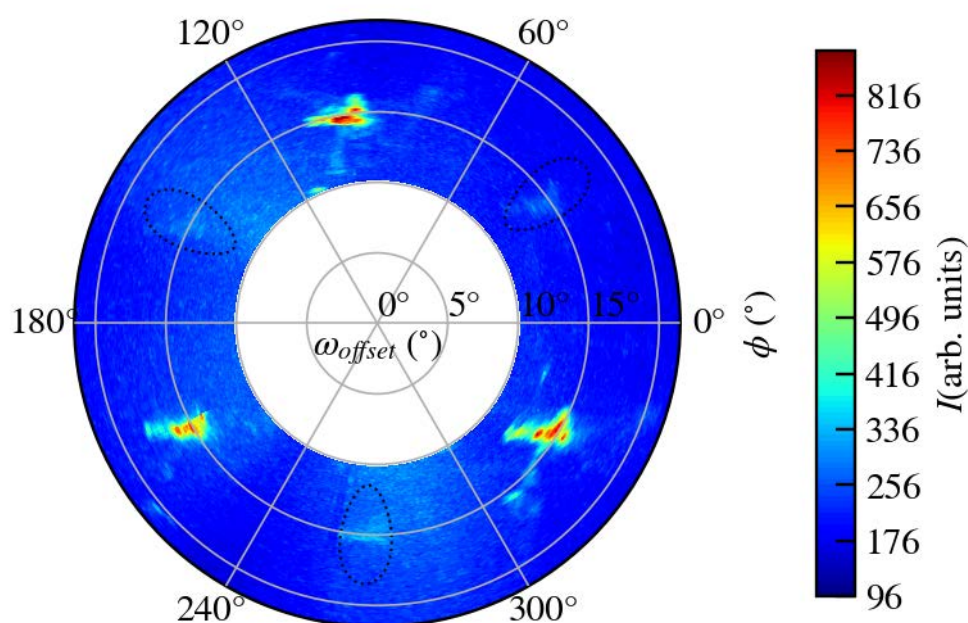


Figure S3| Integrated intensity map. Integrated intensity of HRM in 2θ angle around (1 1 21), (-2 1 21), (1 -2 21) and (2 -1 21), (-1 2 21), (-1 -1 21) diffraction maxima. The 3-fold rotation symmetry is well visible as the (1 1 21), (-2 1 21), (1 -2 21) peaks are more intense than (2 -1 21), (-1 2 21), (-1 -1 21) (enclosed by dashed ellipse) matching the rhombohedral crystal structure model determined in work¹ at 250 K. All diffraction peaks should be separated by 120° in Φ direction. The deviation is caused by limited possibility for sample alignment in a powder diffractometer, which was equipped only by piezo-rotator in Φ direction. Sample on the piezo-rotator was rotated in Φ direction with 1° step. From the Figure it is also well visible the mosaicity of the single crystal, which is around 5° .

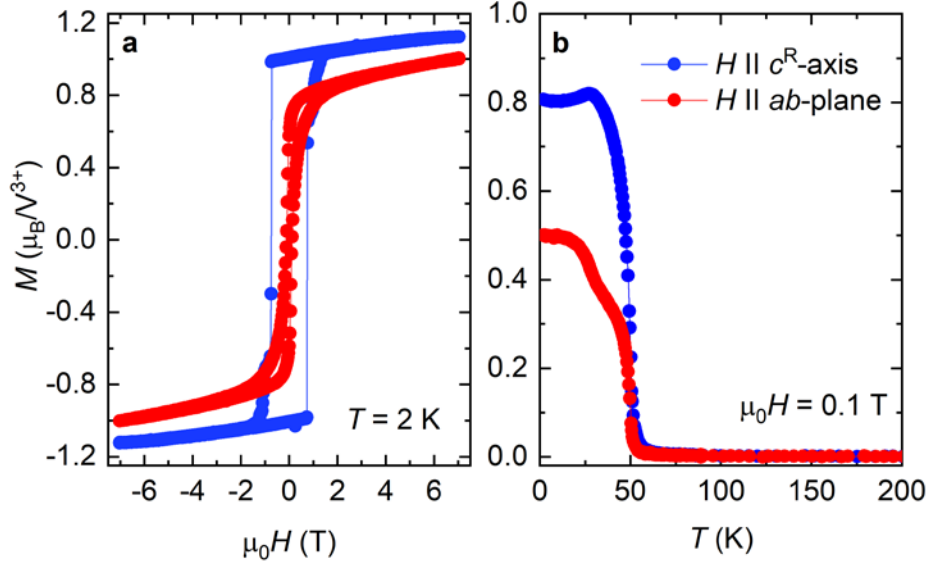


Figure S4| Magnetization measurements of bulk VI₃. **a**, magnetization isotherms measured at $T = 2$ K. The magnetization in $\mu_0 H = 7$ T reaches $1.12 \mu_B/V^{3+}$ along c^R – axis direction and $1 \mu_B/V^{3+}$ along ab -plane direction. **b**, magnetization as a function of temperature measured after field cooling. At $T_C = 50$ K a clear ferromagnetic transition is detected. At around 30 K the ab -plane magnetization projection shows a kink which is related to the order-order phase transition. In the same temperature interval, a small decrease of magnetization along the c^R – axis is observed.

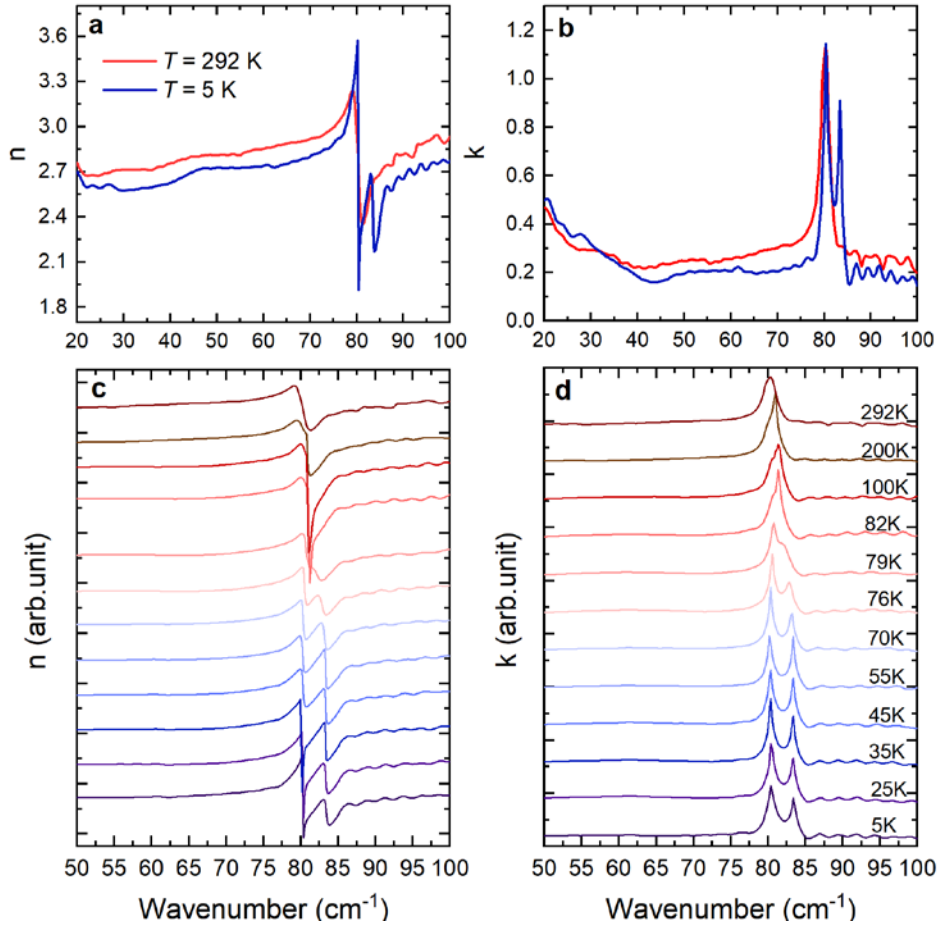
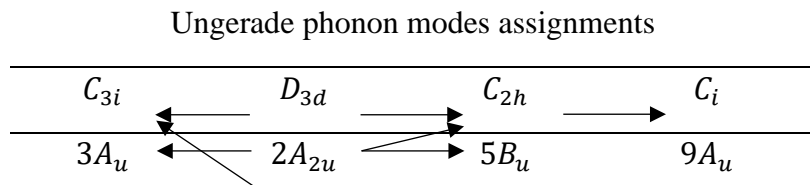


Figure S5| THz spectra measured from room temperature to 5 K. **a**, real part of the refraction index, $n(\omega)$. **b**, imaginary part of the refractive index, $k(\omega)$. We identified a phonon mode around 82 cm^{-1} as an absorption peak and resonance dispersion in the spectral line shape of $k(\omega)$ and $n(\omega)$, respectively. **c,d**, temperature evolution $n(\omega)$ and $k(\omega)$. The splitting of the phonon mode is observed between 82 K and 79K confirming the lowering of the crystal symmetry.



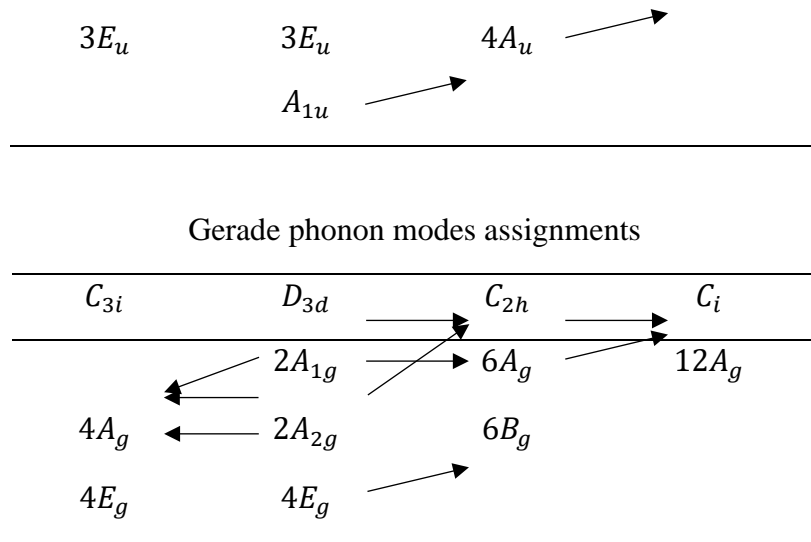


Table S1| The relations between the irreducible representations of different point groups.

The point group $C_{3i}(R\bar{3}$ space group) for trigonal phase and $C_{2h}(C2/m$ space group) for the monoclinic phase do not obey relations group-subgroup. Therefore, no direct correspondence between the irreducible representations (irreps) of the groups exists. However, as the point group of the one triple-layer has higher symmetry which is D_{3d} and is the same for both phases² (the difference between the structure is the triple-layer stacking sequence) we can find in-direct correspondence between the irreps via this point group. The point group C_i for the trigonal phase is the subgroup of the C_{2h} and therefore, the relations between the irreps can be easily find³.

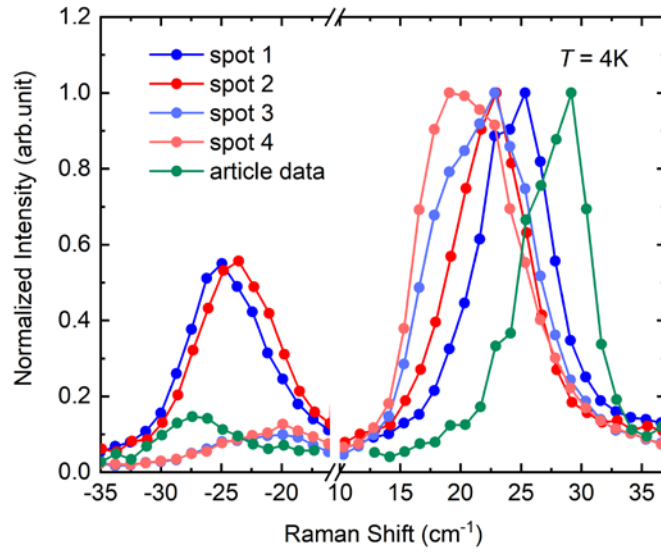


Figure S6| Unpolarized Raman spectrum of the acoustic magnon. We performed testing measurements of the Raman spectra in zero magnetic field which reveal small differences in the magnon frequency depending on the location of the laser spot. The frequency varies from 20 to 29 cm^{-1} . Two Raman spectra (spot 1 and spot 2) show relatively high intensity of the anti-Stokes line compared to the other spectra (each spectrum is normalized such that the magnon peak maximum of the Stokes line is at 1). This might indicate local heating of the sample by the laser, which could cause the frequency shift of the magnon mode. However, as shown in Figure 4b of the main paper, the heating of the sample decreases the magnon frequency which is not observed in our testing spectra. We add that for all spectra we used the same laser power.

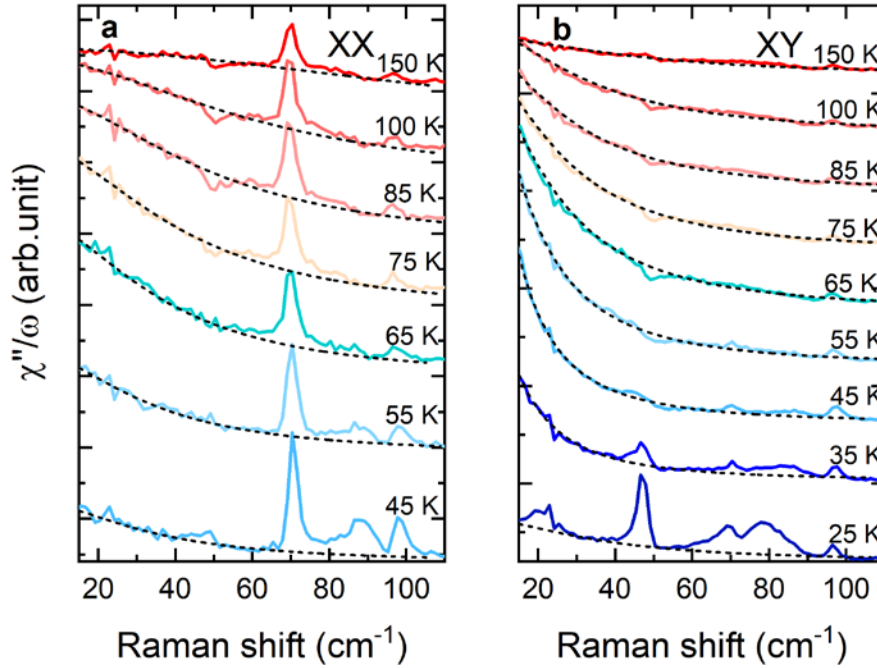


Figure S7| temperature evolution of the Raman conductivity χ''/ω measured in parallel (XX) and crossed (XY) polarization configurations. a,b, The spectra in the temperature interval 150 K – 25 K (45 K for XX channel) were fitted with the Lorentzian function (black dashed lines) with the center of gravity at the Rayleigh line. The peaks and the Fano resonance superposed on the quasi-elastic signal were subtracted before the fitting procedure. To get the spectral weight we integrated the areas below the fits with the integration range of 12-100 cm^{-1} . One should keep in mind, that leaving out a part of the spectral weight (0 – 12 cm^{-1}) slightly decreases the accuracy of the finally established spectral weight values, especially at temperatures where the quasi-elastic scattering peak has small width. The small oscillation at 23 cm^{-1} , which occurs at each temperature in both polarization configuration, does not show any temperature evolution and is considered as an instrumental artifact.

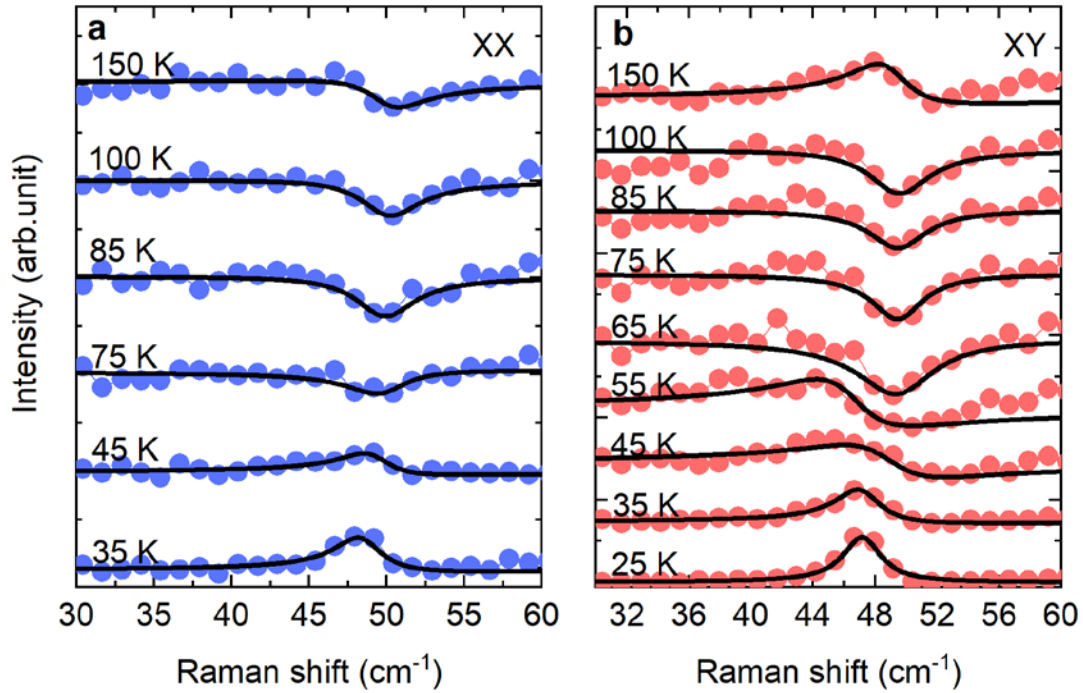


Figure S8| The Raman spectra of the E_g^1 phonon mode. a, for the parallel polarization configuration. **b**, for the crossed polarization configuration (the spectra in the temperature range 150 K - 45 K were multiplied by factor 5 and the spectrum at 35 K by factor 2 for better clarity). The spectra in both configurations were obtained by the subtraction of the quasi-elastic scattering contribution. The solid black lines represent the fits to Equation (9) in the main paper (Fano resonance line shape). We were not able to fit the Raman spectra taken at 55 K and 65 K for the XX polarization configuration by Equation (9) in the main paper as the E_g^1 phonon mode is unresolvable at these temperatures.

References

- (1) Doležal, P.; Kratochvílová, M.; Holý, V.; Čermák, P.; Sechovský, V.; Dušek, M.; Míšek, M.; Chakraborty, T.; Noda, Y.; Son, S.; et al. Crystal structures and phase transitions of the van der Waals ferromagnet Vl_3 . *Physical Review Materials* **2019**, *3* (12), 121401. DOI: 10.1103/PhysRevMaterials.3.121401.
- (2) Larson, D. T.; Kaxiras, E. Raman spectrum of CrI_3 : An *ab initio* study. *Physical Review B* **2018**, *98* (8), 085406. DOI: 10.1103/PhysRevB.98.085406.

(3) Aroyo, M. I.; Kirov, A.; Capillas, C.; Perez-Mato, J. M.; Wondratschek, H. Bilbao Crystallographic Server. II. Representations of crystallographic point groups and space groups. *Acta Crystallographica Section A* **2006**, *62* (2), 115-128. DOI: doi:10.1107/S0108767305040286.